



HAL
open science

Boosting the performances of semitransparent organic photovoltaics via synergetic near-infrared light management

Tao Xu, Baozhong Deng, Kaiwen Zheng, Hongyu Li, Zihan Wang, Yunbo Zhong, Chengxi Zhang, Gaëtan Lévêque, Bruno Grandidier, Renaud Bachelot, et al.

► To cite this version:

Tao Xu, Baozhong Deng, Kaiwen Zheng, Hongyu Li, Zihan Wang, et al.. Boosting the performances of semitransparent organic photovoltaics via synergetic near-infrared light management. *Advanced Materials*, 2024, 36 (18), pp.2311305. 10.1002/adma.202311305 . hal-04465431

HAL Id: hal-04465431

<https://hal.science/hal-04465431v1>

Submitted on 7 May 2024

HAL is a multi-disciplinary open access archive for the deposit and dissemination of scientific research documents, whether they are published or not. The documents may come from teaching and research institutions in France or abroad, or from public or private research centers.

L'archive ouverte pluridisciplinaire **HAL**, est destinée au dépôt et à la diffusion de documents scientifiques de niveau recherche, publiés ou non, émanant des établissements d'enseignement et de recherche français ou étrangers, des laboratoires publics ou privés.

Boosting the Performances of Semitransparent Organic Photovoltaics via Synergetic Near-Infrared Light Management

Tao Xu, Baozhong Deng, Kaiwen Zheng, Hongyu Li, Zihan Wang, Yunbo Zhong, Chengxi Zhang, Gaëtan Lévêque, Bruno Grandidier, Renaud Bachelot, Mona Treguer-Delapierre,* Yabing Qi,* and Shenghao Wang*

Semitransparent organic photovoltaics (ST-OPVs) offer promising prospects for application in building-integrated photovoltaic systems and greenhouses, but further improvement of their performance faces a delicate trade-off between the two competing indexes of power conversion efficiency (PCE) and average visible transmittance (AVT). Herein, the authors take advantage of coupling plasmonics with the optical design of ST-OPVs to enhance near-infrared absorption and hence simultaneously improve efficiency and visible transparency to the maximum extent. By integrating core–birefringent PdCu@Au@SiO₂ nanotriprisms that act as optically isotropic Lambertian sources with near-infrared-customized localized surface plasmon resonance in an optimal ternary PM6:BTP-eC9:L8-BO-based ST-OPV, it is shown that their interplay with a multilayer optical coupling layer, consisting of ZnS(130 nm)/Na₃AlF₆(60 nm)/WO₃(100 nm)/LaF₃(50 nm) identified from high-throughput optical screening, leads to a record-high PCE of 16.14% (certified as 15.90%) along with an excellent AVT of 33.02%. The strong enhancement of the light utilization efficiency by ≈50% as compared to the counterpart device without optical engineering provides an encouraging and universal pathway for promoting breakthroughs in ST-OPVs from meticulous optical design.

1. Introduction

Transparent photovoltaics, which combines solar energy conversion and light transmittance at visible wavelengths, are becoming a key technology to turn ubiquitous glass windows into active solar panels in buildings, vehicles, and greenhouses.^[1–5] One of the main challenges consists in maximizing the optical absorption in the near-infrared (NIR) portion of sunlight that represents over 50% of solar energy so that the power conversion efficiency (PCE) does not decrease at the expense of the average visible transmittance (AVT).^[6,7] To track progress among different materials and structures that aim at enhancing simultaneously AVT and PCE, the light utilization efficiency (LUE) that corresponds to the product of PCE and AVT values, has emerged as a key figure of merit.^[8] To date, semitransparent organic photovoltaics (ST-OPVs) show the highest LUE values and represent the best candidate

T. Xu, B. Deng, K. Zheng, H. Li, Z. Wang, S. Wang
School of Microelectronics and Materials Genome Institute
Shanghai University
Shanghai 200444, China
E-mail: shenghaowang@shu.edu.cn

Y. Zhong
School of Materials Science and Engineering
Shanghai University
Shanghai 200444, China

C. Zhang
School of Science
Jiangsu University of Science and Technology
Zhenjiang 212100, China

G. Lévêque, B. Grandidier
Univ. Lille
CNRS
Centrale Lille
Univ. Polytechnique Hauts-de-France
Junia-ISEN
UMR 8520 – IEMN
Lille 59000, France

R. Bachelot
Light
nanomaterials
nanotechnologies (L2n)
CNRS ERL 7004
University of Technology of Troyes
Troyes F-10004, France

R. Bachelot
EEE School
Nanyang Technological University
CNRS IRL, CINTRA 3288, Singapore

 The ORCID identification number(s) for the author(s) of this article can be found under <https://doi.org/10.1002/adma.202311305>

for transparent photovoltaic applications, taking advantage of the recent progress in nonfullerene acceptors (NFAs).^[9–16] In contrast to their inorganic counterparts, the absorption bands of organic semiconductors are discrete and, if cleverly engineered, predominantly absorb NIR wavelengths, allowing transparency in the visible range. In addition to several advantages including low cost, flexibility, and solution processability,^[17–21] their structures are well-suited for light management engineering using various photonic structures, such as photonic crystals and dielectric mirrors, which provides a facile way to improve the PCE while optimizing the light transmission with designed spectra.^[22–25] In particular, optical coupling layers (OCL) have been employed on transparent electrodes to manipulate the light field distribution in the device, thus improving the LUE of ST-OPVs.^[26–28] Promising progress in the structural optimization of OCL has been recently obtained using high-throughput optical screening to achieve the absolute maximum of critical indexes for ST-OPVs.^[29–31] However, despite these improvements and the innovations of the absorbing materials to minimize energy losses, the experimental LUE lags behind the theoretical prediction, calling for a more elaborate optical design in trapping NIR photons.

Another effective method of light management is to use plasmonic metal nanostructures (MNS) as subwavelength light concentrators for enhancing light harvesting via localized surface plasmon resonance (LSPR).^[32–34] Despite the numerous studies reported on the integration of MNS with various shapes, sizes, and compositions in OPVs,^[35–40] extended application of MNS with LSPR in the NIR wavelength range for ST-OPVs has rarely been undertaken. Indeed, two major hurdles need to be overcome. First, the LSPR must precisely match the absorption range of NFAs, requiring a high degree of control in shaping the MNS that is also needed to control the light scattering. Second, exciton quenching at the surface of the embedded MNS must be avoided, imposing the encapsulation of a dielectric shell on the MNS, which inhibits charge recombination yet retains attractive optical properties.^[41–43]

In this work, a strategy for enhanced NIR light management relying on plasmonic effects combined with OCL and anti-reflection (AR) coating is proposed, as described in **Figure 1**. Guided by theoretical simulation and synthesis optimization, core–shell PdCu@Au@SiO₂ nanotriangles (NTPs) with deliberately customized LSPR in the NIR region were introduced in the ternary bulk heterojunction (BHJ) active layer of PM6:BTP-eC9:L8-BO. Acting as optically isotropic Lambertian sources, we show that the synergy

of the NTPs with an optimized multilayer OCL consisting of ZnS(130 nm)/Na₃AlF₆(60 nm)/WO₃(100 nm)/LaF₃(50 nm), identified from high-throughput screening of ≈40 000 000 different device configurations, improves the NIR light utilization to the greatest extent. Taking advantage of an additional nanostructured AR coating, a record-high PCE of 16.14% (15.90% certified) along with an excellent AVT of 33.02% were obtained, leading to an outstanding LUE of 5.33%, among the highest achieved values in ST-OPVs. Moreover, the synergistic strategy developed in this work is suitable to withstand a long operational lifetime, with device stability exceeding $T_{90} > 1000$ h.

2. Results and Discussion

A set of ST-OPVs, used as a control device for comparative studies, was first fabricated and consisted of the following structure: indium tin oxide (ITO)/poly(3,4-ethylenedioxythiophene): poly(styrene sulfonate) (PEDOT: PSS)/BHJ/poly[[2,7-bis(2-ethylhexyl)–1,2,3,6,7,8-hexahydro-1,3,6,8-tetraoxobenzol[*lmn*][3,8]phenanthroline-4,9-diyl]–2,5-thiophenediyl[9,9-bis[3-(dimethylamino)propyl]–9H-fluorene-2,7-diyl]–2,5-thiophenediyl] (PNDIT-F3N)/Au/Ag. The 30 nm-thick PEDOT: PSS, 10 nm-thick PNDIT-F3N, and bilayer Au (1 nm)/Ag (10 nm) were used as the hole transport layer (HTL), electron transport layer (ETL) and upper semitransparent electrode, respectively, to ensure charge collection in the ST-OPVs. The addition of an ultrathin Au interlayer improves the wettability of the upper Ag contact and transforms the growth mode of the thin Ag layer from the 3D Stranski–Krastanov mode to the 2D Frank–van der Merwe mode, thereby favoring formation of a uniform transparent upper Au (1 nm)/Ag (10 nm) electrode, as shown in the scanning electron microscope (SEM) observations of **Figure S1** (Supporting Information), which is consistent with previous reports.^[44,45] It should be noted that PEDOT: PSS was modified by using Nb₂C MXene to improve the conductivity of HTL and the photovoltaic performance, as reported in our previous work.^[46] A ternary blend film of PM6:BTP-eC9:L8-BO was used as the BHJ active layer, taking advantage of the high PCE obtained by this ternary system in opaque OPVs.^[47]

PM6 exhibits strong absorption in the visible region that overlaps with the human eye response, whereas BTP-eC9 and L8-BO display complementary absorption in the NIR region (**Figure S2a**, Supporting Information). Considering the requirement of limited absorption in the visible wavelength range, the weight ratio of PM6 to BTP-eC9 to L8-BO in the BHJ was optimized to improve the LUE (LUE = PCE × AVT). The absorption spectra of the BHJ films with different weight ratios of PM6 to BTP-eC9 to L8-BO reveal that a low PM6 content is beneficial for visible transmission (**Figure S2b**, Supporting Information). The current density–voltage (*J*–*V*) characteristics, external quantum efficiency (EQE), and transmission spectra of the ST-OPVs were first characterized for a 140 nm-thick BHJ active layer, using different weight ratios of PM6 to BTP-eC9 to L8-BO of 1.0:0.4:0.8, 0.8:0.4:0.8, 0.6:0.4:0.8, and 0.4:0.4:0.8 (**Figure S3**, Supporting Information). The corresponding short-circuit current density (J_{SC}), open circuit voltage (V_{OC}), fill factor (FF) and PCE are listed in

M. Treguer-Delapierre
Univ. Bordeaux
CNRS
Bordeaux INP
ICMCB
UMR 5026, Pessac F-33600, France
E-mail: mona.treguer@icmcb.cnrs.fr

Y. Qi
Energy Materials and Surface Sciences Unit (EMSSU)
Okinawa Institute of Science and Technology Graduate University (OIST)
1919-1 Tancha, Onna-son, Okinawa 904-0495, Japan
E-mail: Yabing.Qi@OIST.jp

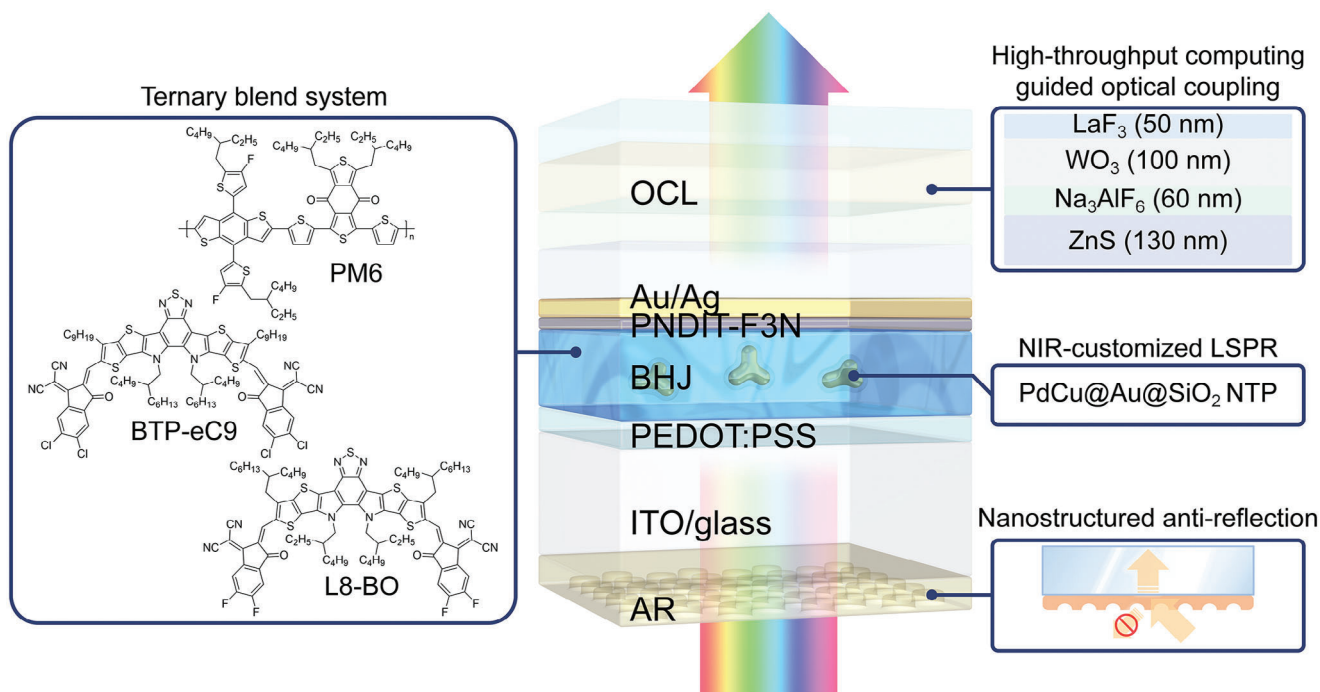


Figure 1. A schematic diagram of the synergetic light management strategy is demonstrated in this work.

Table S1 (Supporting Information). The AVT of the ST-OPVs is calculated using the following equation:

$$AVT = \frac{\int_{370}^{740} T(\lambda) V(\lambda) F(\lambda) d\lambda}{\int_{370}^{740} V(\lambda) F(\lambda) d\lambda} \quad (1)$$

where $T(\lambda)$ is the transmission spectrum of the ST-OPVs, $V(\lambda)$ is the human eye response spectrum and $F(\lambda)$ is the power irradiation of AM1.5G. The highest LUE of 3.23%, with a PCE of 13.67% and an AVT of 23.6%, was obtained for ST-OPVs with a weight ratio of PM6 to BTP-eC9 to L8-BO of 0.6:0.4:0.8. Furthermore, the thickness of the BHJ active layer was delicately adjusted to optimize the performance of the ST-OPVs over the two competing indexes of PCE and AVT. PM6:BTP-eC9:L8-BO (0.6:0.4:0.8)-based ST-OPVs with different BHJ thicknesses of 140, 120, 100 and 80 nm were subsequently fabricated. The $J-V$ characteristics, EQE, and transmission spectra are shown in Figure S4 (Supporting Information) and the photovoltaic parameters are listed in Table S2 (Supporting Information). Finally, the PM6:BTP-eC9:L8-BO (0.6:0.4:0.8)-based ST-OPVs with a 100 nm-thick BHJ yield a PCE of 13.33%, an AVT of 27.45% and an optimized LUE of 3.65%, which are used as reference values. Such performance is comparable to that of ST-OPVs using donors with narrow bandgap.^[48,49]

2.1. OCL ST-OPVs with PdCu@Au@SiO₂ NTPs

To further improve the photovoltaic performance of ST-OPVs, a subtly designed core–bishell plasmonic MNS of PdCu@Au@SiO₂ NTPs with NIR-customized LSPR was introduced into the BHJ active layer to achieve NIR absorption

enhancement and scattering optimization. PdCu@Au@SiO₂ NTPs were synthesized by a multiple-step synthesis including inorganic growth, metal deposition, and silica encapsulation, as described in Figure S5 (Supporting Information) and the Experimental Section.^[50] A uniform Au shell of controlled thickness was grown on the pre-synthesized PdCu seeds with three branches, followed by another ultrathin silica coating to form core–bishell NTPs. Finally, delicate surface functionalization with an organo-silane coupling agent, such as octadecyltrimethoxysilane (OTMS), was performed to ensure good dispersion and colloidal stability of the NTPs in the organic solution and film, as reported in some previous works.^[36,51] The dispersion of the NTPs can be evidenced in Figure S6 (Supporting Information). Transmission electron microscopy (TEM) analysis of the NTPs shows good control of the fabrication procedure by taking advantage of the low dispersity of the PdCu synthesis reaction and the precision of the seeded-growth for Au and silica plating techniques. In addition, the stability was confirmed by unchanged spectra of the NTPs after 6 months of storage in chloroform (Figure S7, Supporting Information). The size distribution of the PdCu seeds and the PdCu@Au NTPs (Figure S8, Supporting Information) reveals the key features of our synthetic approach: a high degree of control over morphology ($\approx 80\%$ yield) and the ability to scale up the fabrication to bulk quantities. More importantly, it is worth mentioning that the thickness of the Au shell can be precisely tuned during the synthesis to gain good control over the geometrical parameters of the NTPs and thus their optical properties. Figure 2a shows a high-resolution transmission electron microscope (HRTEM) image of a typical PdCu@Au@SiO₂ NTP with three equiangular branches and a high-angle annular dark field (HAADF) image where the PdCu seed is seen to be entirely covered by the Au shell. The

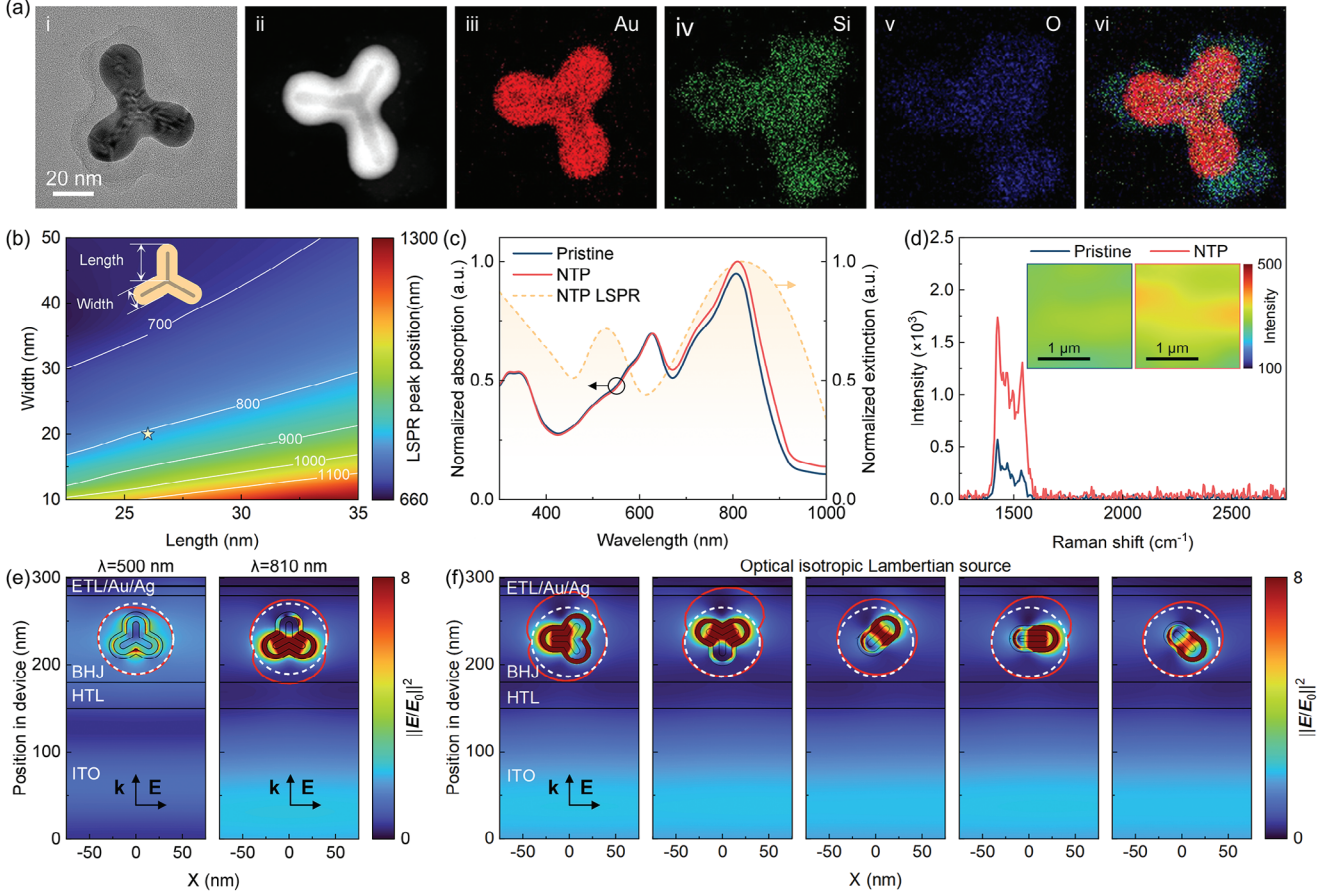


Figure 2. a) HRTEM image (panel i), HAADF STEM image (panel ii), and EDS elemental mappings of Au, Si, and O elements (panels iii–v) as well as the superimposed mapping for a PdCu@Au@SiO₂ NTP (panel vi). b) Contour map of the peak wavelength of the NTP-induced LSPR as a function of the width and length of NTPs. The star symbol stands for the experimental result. Inset: schematic diagram illustrating the geometrical parameters of a NTP. c) Normalized absorption spectra measured for the pristine BHJ film (solid blue curve) and the hybrid BHJ film with NTPs (solid red curve) and normalized extinction spectra of NTPs in chloroform (dashed yellow curve). d) Raman spectra measured for the pristine BHJ film and the hybrid BHJ film with NTPs. Inset: corresponding Raman mappings with a size of $2 \times 2 \mu\text{m}^2$, probed at 1425 cm^{-1} . e) Distributions of the electric field intensity inside the ST-OPVs with NTPs at excitation wavelengths of 500 and 810 nm. The scattering diagrams, plotted in red around NTPs, represent the amplitude of the Poynting vector \vec{P} along the white-dashed ellipsoids. f) Distributions of the electric field intensity inside the ST-OPVs with the presence of NTPs in the BHJ active layer under different rotation angles at an excitation wavelength of 810 nm.

energy-dispersive spectroscopy (EDS) mappings of Au, Si, and O elements confirm the presence of a homogeneous silica shell with a thickness of $\approx 8 \text{ nm}$ around the NTP. It should be noted that the presence of such a silica coating can effectively prevent undesired exciton quenching between the metallic surface and organic semiconductor, while the thickness needs to be thin enough to preserve the plasmonic optical properties.^[52]

To obtain a precise degree of control over the NTP-induced LSPR for achieving the NIR absorption enhancement in ST-OPVs, the correlation of the resonance wavelength of the LSPR and the geometrical parameters of the NTPs was analyzed by using finite element method simulations. Figure 2b shows the simulated evolution of the peak wavelength of the NTP-induced LSPR as a function of the width and length of each branch of the NTPs, revealing that the peak wavelength of the NTP-induced LSPR can be tuned from 600 to 1200 nm by designing an appropriate shape. In our case, a NIR-LSPR peak position of $\approx 810 \text{ nm}$

is needed to match the dominant absorption range of the BHJ active layer in ST-OPVs. Following the simulated prediction, NTPs with a branch width of 20 nm and a branch length of 26 nm were synthesized, yielding an experimental LSPR peak wavelength of 811 nm labeled as the star symbol in Figure 2b. After coating a thin silica film, the spectrum of the core–shell NTPs was found to be slightly red-shifted to 820 nm and broadened, as shown in Figure S9 (Supporting Information), which can be attributed to the increase of refractive index caused by the silica coating and the increased damping of collective electron oscillations.^[53–55]

By integrating the PdCu@Au@SiO₂ NTPs in the BHJ film, the absorption of the hybrid film is evidently enhanced in the NIR wavelength range from 700 to 900 nm as shown in Figure 2c. Besides, the visible transmission of the BHJ film is not affected by the presence of the NTPs (Figure S10, Supporting Information). This fact can be explained by the respective contribution of the two plasmonic peaks. The NTP can be characterized by

two radii: an inner radius covering the NTP core ($R^1 \approx 10$ nm) and an external radius ($R^2 \approx 40$ nm), as shown in Figure S11a (Supporting Information), which corresponds to the plasmonic extinction peaks in the visible and in the NIR wavelength range, respectively. According to the Mie–Rayleigh theory, the scattering cross section of MNS with size R is proportional to R^6 while the absorption cross section is proportional to the nanoparticle volume (R^3).^[56] As a result, only the resonant plasmonic mode in the NIR leads to significant scattering within the active layer, which was confirmed by the scattering spectra measured on a single NTP (Figure S11b, Supporting Information), resulting in an increase of the optical path and an enhanced absorption of the NIR photons in the BHJ active layer. Finally, it should be mentioned that the absorption of the incident light by the NTPs is limited, considering the small concentration (0.1 wt.%) of the NTPs in the BHJ active layer. These results suggest that the incorporation of the NTPs in the BHJ film can help enhance the NIR absorption without notably changing the AVT of the ST-OPVs.

The morphological properties of the hybrid BHJ film with NTPs were then studied using TEM. High contrast regions (marked by the white circles in Figure S12, Supporting Information) were observed in the hybrid film, providing evidence of the successful incorporation of NTPs in the BHJ film with good dispersion. Interestingly, the morphology of the film is not affected, as similar surface morphologies and root-mean-square (RMS) roughness values were measured by using atomic force microscopy (AFM) for films with and without NTPs (Figure S13, Supporting Information). The molecular orientation and crystalline properties of both types of films were also investigated by using grazing incidence wide-angle X-ray scattering (GIWAXS). Similar face-on orientation structures with an evident scattering in the out-of-plan direction (1.71 \AA^{-1}) and in-plane direction (0.34 \AA^{-1}) were observed for both films (Figure S14, Supporting Information), which represent the (010) π - π stacking and (100) lamellar stacking. The π - π stacking d-spacing in the out-of-plane direction of the BHJ film with NTPs is 3.678 \AA , which is very close to that of the pristine BHJ film (3.674 \AA). In addition, the introduction of NTPs does not affect the lamellar crystal coherence length in the in-plane direction (43.83 \AA vs 44.17 \AA of the pristine active layer), indicating that the molecular packing and crystallinity of the BHJ active layer are not degraded by integrating NTPs (Table S3, Note S1, Supporting Information). In addition to these morphological observations, Figure 2d shows the typical Raman spectra measured for the pristine and hybrid films. The peaks located between 1400 and 1550 cm^{-1} correspond to the C=C stretching vibration of the thiophene ring. A stronger peak intensity was observed for the hybrid film, which can be explained by the surface-enhanced Raman scattering induced by the presence of NTPs.^[57] Raman mapping with a size of $2 \times 2 \text{ \mu m}^2$ shown in the inset of Figure 2d, tracking the maximum peak intensity, illustrates regions with higher intensity in the hybrid film, further confirming the integration of NTPs in the BHJ film. The broader distribution of Raman peak intensity in the hybrid film (Figure S15, Supporting Information) indicates that NTPs are randomly distributed in the BHJ active layer.

The mechanism of the NIR absorption enhancement in the NTP-based ST-OPVs was investigated numerically, on the basis

of the optimized geometrical parameters of the NTPs. Figure 2e shows the distribution of the electric field intensity in the ST-OPVs with the presence of NTPs in the BHJ, at excitation wavelengths of 500 nm (transverse polarization) and 810 nm (longitudinal polarization). It is clear that strong near-field enhancement and hot-spot effect around the NTP are manifested at 810 nm , which is beneficial for NIR absorption enhancement in the ST-OPVs. In addition to near-field enhancement, NTPs can behave as antennas for light scattering, increasing the optical path and thus boosting the absorption of the NIR photons in the BHJ active layer. To evaluate the antenna effect, the scattering was characterized by evaluating the time-averaged Poynting vector, using the following equation:

$$\vec{\Pi}(\vec{r}, \omega) = \frac{1}{2} \text{Re} \left\{ \vec{E}(\vec{r}, \omega) \times \vec{H}^*(\vec{r}, \omega) \right\} \quad (2)$$

where \vec{H} is the magnetic field. The vector $\vec{\Pi}$ was calculated numerically along the white dashed ellipsoid, while the red line indicates the location of the extremities of Poynting's vector starting on the ellipsoids. The Poynting vector that carries the radiated photonic energy is found to be enhanced in the NIR wavelength at 810 nm , close to the longitudinal dipolar plasmon. Even if most of the scattering occurs in the direction perpendicular to the BHJ active layer due to the particular orientation of the NTP in Figure 2e, a significant proportion of light propagates at larger angles in the direction of the BHJ active layer. As the NTPs are expected to be randomly positioned inside the experimental device, we have investigated the effect of the angular distribution of the NTPs on the direction of the scattering. Simulations for NTPs in the BHJ active layer with different rotation angles and the corresponding Poynting vectors are calculated, as shown in Figure 2f and Figure S16 (Supporting Information). It can be observed that the Poynting vectors are constantly enhanced at the resonance wavelength where the orientation is arbitrary. Except in configurations where the NTP axis is perpendicular to the layers of the OPV, the maximum scattering generally occurs along directions quasi parallel to the horizontal direction, increasing the time that light passes inside the BHJ active layer and thus enhancing the corresponding absorption. On average, due to the specific symmetry of the NTPs that is characterized by the D_{3h} point group,^[58] the incident light is scattered isotropically in the BHJ active layer despite the random orientations of the NTPs. The NTPs act as efficient Lambertian nanosources to produce a far-field whose apparent brightness to an observer is roughly the same regardless of the observer's angle of view.^[59] As a result, statistically, the optical path of light within the active layer is expected to increase in every direction of space, which leads to an increase in the effective absorption and resulting photocurrent.^[60] In summary, those simulation results unveil that the optically amplified field near the vicinity of NTPs, the enhanced light scattering, and their mutual coupling are likely to enable the NIR absorption enhancement in the BHJ active layer.

To validate the aforementioned physical picture, a set of NTP-based ST-OPVs with different concentrations of NTPs in the BHJ active layer was fabricated. Based on the characterization of the devices (Figure S17, Table S4, Supporting Information), the use of PdCu@Au@SiO_2 NTPs is found to be beneficial for the

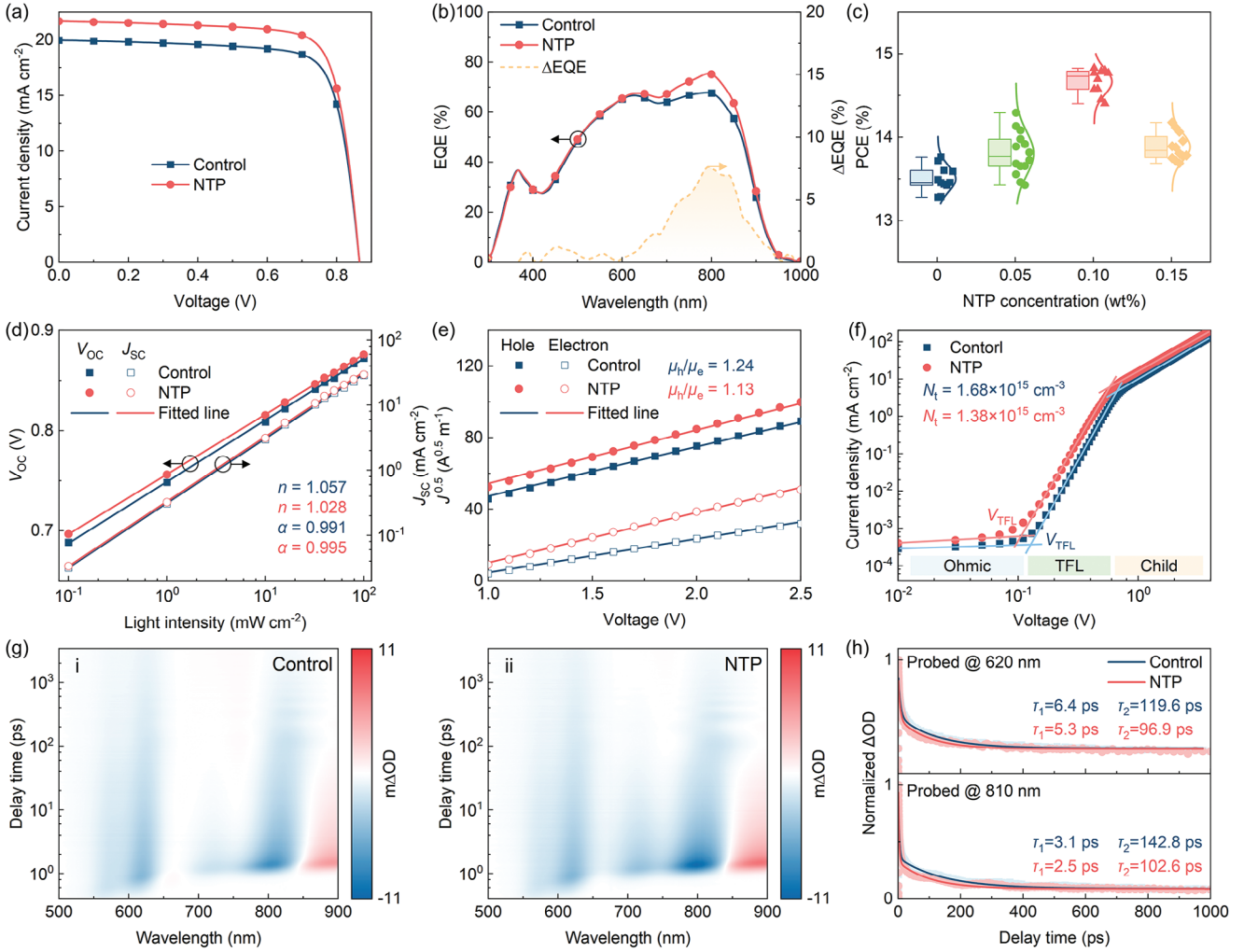


Figure 3. a) J - V characteristics of the ST-OPVs with a 100 nm-thick PM6:BTP-eC9:L8-BO(0.6:0.4:0.8)-based BHJ with and without NTPs. b) EQE spectra of the ST-OPVs with a 100 nm-thick PM6:BTP-eC9:L8-BO(0.6:0.4:0.8)-based BHJ with (solid red curve) and without (solid blue curve) NTPs, and EQE difference (dashed yellow curve) between devices with and without NTPs. c) PCE distribution of ST-OPVs with different concentrations of NTPs in the BHJ active layer. d) V_{OC} - I and J_{SC} - I measurement results. e) Carrier mobilities results and f) trap density for the control device and the ST-OPVs with NTPs by SCLC measurement. g) The 2D TA profile of the 100 nm-thick PM6:BTP-eC9:L8-BO(0.6:0.4:0.8)-based BHJ without (panel i) and with NTPs (panel ii). h) TA dynamics of the GSB signals probed at 620 and 810 nm for the BHJ films with and without NTPs.

enhancement of the device performance. An optimal concentration of NTPs in the BHJ active layer at 0.1 wt.% leads to the highest PCE of 14.66%, while the AVT is well maintained at 27.4%, giving an improved LUE of 4.02%. J - V characteristics and the corresponding EQE spectra measured for a control ST-OPV with a pristine BHJ active layer and the ST-OPV with an optimal hybrid BHJ film are shown in **Figure 3a** and **Figure 3b**. The results clearly reveal that the NTP-assisted NIR absorption enhancement is mainly due to the increase in EQE of the NTP-based ST-OPVs over the NIR wavelength range from 700 to 900 nm, originated from the combined effects of the NTPs-induced LSPR and scattering, which agrees well with the previous theoretical simulation. In addition, the reflectance spectra and the EQE + T + R spectra were measured for ST-OPVs with and without NTPs to reveal the light utilization of the device (**Figure S18**, Supporting Information), indicating that the use of the NTPs enables boosting the NIR absorption in the active layer without a trade-off in

the transparency of the ST-OPVs. To ensure the reproducibility and reliability of our results, the distribution of PCE values for ST-OPVs with different concentrations of NTPs in the BHJ active layer is plotted in **Figure 3c**, giving a reasonable narrow standard deviation.

To get a deep insight into the electrical effect of NTPs on the enhancement of photovoltaic performance in ST-OPVs, the exciton dissociation, charge recombination, and collection properties were systematically studied. The photocurrent density (J_{ph})-effective voltage (V_{eff}) characteristics of the ST-OPVs with and without NTPs in the BHJ active layer were measured and plotted in **Figures S19,S20** (Supporting Information) to analyze the exciton dissociation properties of the devices. The exciton dissociation probability (P_{diss}) is calculated as described in **Note S2** (Supporting Information). The NTP-based device shows a higher P_{diss} of 98.7% compared with that of the control device (97.3%). The charge recombination in the ST-OPVs was further

investigated using the light intensity (I) dependence test, as shown in Figure 3d. The factors α and n fitted from the $J_{sc}-I$ and $V_{oc}-I$ curves are calculated as described in Note S3 (Supporting Information). An exponent α of 0.995 is obtained for the NTP-based device, which is slightly higher than that of the control device (0.991), indicating that the addition of NTPs can improve charge extraction in the ST-OPVs. Meanwhile, the NTP-based device shows a lower n value of 1.028 than that of the control device (1.057), suggesting that monomolecular recombination is suppressed.^[61] The contact resistance and bulk resistance of the ST-OPVs were analyzed by using electrochemical impedance spectroscopy, and the corresponding Nyquist plot is shown in Figure S21 (Supporting Information). The NTPs-based device exhibits lower R_s of 10.8 Ω and R_p of 216.6 Ω compared with those of the control device ($R_s = 19.1 \Omega$ and $R_p = 406.4 \Omega$), which indicates lower transport resistance and interfacial barriers in the device, thus increasing the carrier mobility. Hence, the carrier mobility was measured by using the space-charge-limited current (SCLC) method, as shown in Figure 3e. Hole-only devices and electron-only devices with and without NTPs were fabricated to calculate the hole mobility (μ_h) and electron mobility (μ_e), as described in Note S4 (Supporting Information). The detailed values of μ_h and μ_e are summarized in Table S5 (Supporting Information). A more balanced μ_h/μ_e value of 1.13 is obtained for the NTP-based device compared with that of the control device (1.24), which suggests better percolation pathways for the charge carriers, leading to a minimized space-charge region and suppressed bimolecular recombination.^[62] Furthermore, the trap density (N_t) in the BHJ active layer was investigated via SCLC measurements as shown in Figure 3i, which is calculated as described in Note S5 (Supporting Information). The NTP-based device exhibits a lower trap-filled limit voltage (V_{TFL}), suggesting a lower N_t of $1.38 \times 10^{15} \text{ cm}^{-3}$ as compared to that of the control device ($1.68 \times 10^{15} \text{ cm}^{-3}$). Indeed, the plasmonic effect of NTPs can help generate hot-carriers to fill the trap states and substantially improve the charge transport in OPVs.^[32]

The photoinduced charge transfer dynamics were further investigated by using transient absorption (TA) measurements. As shown in Figure 3,h, the ground state bleaching (GSB) signal of PM6 appears at 620 nm, while that of NFAs appears at 810 nm. Compared with the control BHJ film, the hybrid film with NTPs shows a higher signal intensity, indicating enhanced carrier transport. The hole and electron transport kinetics are then numerically analyzed by fitting the PM6 GSB signal (620 nm) and the NFA GSB signal (810 nm), respectively, as shown in Figure 3i and Figure S22 (Supporting Information). The charge transport involves a fast process lifetime τ_1 that is related to the exciton dissociation time, and a slow process lifetime τ_2 assigned to the exciton diffusion and recombination time. The τ_1 and τ_2 of the hybrid film with NTPs are calculated to be 5.3 and 96.9 ps for hole transport, shorter than those of the control BHJ film (6.4 and 119.6 ps), while similar shorter lifetimes for electron transport are obtained in the hybrid film, indicating more rapid exciton dissociation at the donor–acceptor interfaces.^[63] In summary, these results demonstrate that the incorporation of the PdCu@Au@SiO₂ NTPs can help accelerate the charge transfer kinetics and enhancing the charge extraction through mitigation of the charge recombination, thereby yielding a higher J_{sc} and PCE in ST-OPVs.

2.2. ST-OPVs with a Multilayer OCL

To further improve the performance of ST-OPVs over the two competing indexes of PCE and AVT, a multilayer OCL was applied on top of the Au/Ag semitransparent electrode. High-throughput optical screening based on the transfer matrix method (TMM) was developed to comprehensively evaluate the optical coupling effect in ST-OPVs, with the aim of improving the visible light transparency and NIR absorption simultaneously. The wavelength-dependent refractive index and extinction coefficient of the functional layers used in the simulation were measured using an ellipsometer (Figure S23, Supporting Information). The detailed simulation methods are described in the Experimental Section. Based on the refractive indexes and geometrical parameters of each functional layer, the optical model allows us to compute the distribution of the electromagnetic field in the ST-OPVs, together with the reflection, transmission, and absorption in the BHJ active layer, which helps calculating the key parameters of ST-OPVs, such as J_{sc} and AVT. Figure 4a illustrates the cross-sectional view of an OCL-integrated ST-OPV with the potential dielectric material of the OCL noted as the refractive index n_1, n_2, n_3 , and n_4 , and the possible layer thickness of the OCL described as d_1, d_2, d_3 and d_4 . High-throughput optical screening for predicting the best configuration of OCL was subsequently performed, in which the refractive index was varied over the range from 1.0 to 3.0 with an interval of 0.1, and the corresponding layer thicknesses were varied over the range from 0 to 200 nm with an interval of 10 nm. A total of 47 064 402 device configurations were simulated through permutations of thickness variables and refractive index variables to reach the optical coupling enhancement in ST-OPVs to the maximum extent.

Figure 4b shows a contour map of J_{sc} and AVT as a function of the refractive index and the layer thickness of the OCL. Despite the inevitable trade-off between J_{sc} and AVT in ST-OPVs, the high-throughput optical screening reveals that the performance of the ST-OPVs can be optimized by incorporating an appropriate OCL with the best material choice and the optimized thickness in the direction of the arrow where the two competing indexes can be simultaneously improved. Both bilayer OCL labeled as blue points and multilayer OCL labeled as red points were analyzed. The multilayer OCL extends the theoretical limit compared with that of the bilayer OCL, which is beneficial for achieving higher J_{sc} and AVT. The inset of Figure 4b shows the magnified part for the chart of coordinates in which the theoretical limit is indicated as the blue fitted line for bilayer OCL and the red fitted line for multilayer OCL. In the contour map of Figure 4b, the circle symbol (labeled Control; cyan color) represents the J_{sc} and AVT values calculated for the control device without OCL. The simulated results indicate an optimal multiple OCL configuration of $(n_1 = 2.4, d_1 = 130 \text{ nm})/(n_2 = 1.3, d_2 = 60 \text{ nm})/(n_3 = 2.0, d_3 = 100 \text{ nm})/(n_4 = 1.6, d_4 = 50 \text{ nm})$. Among the realistic dielectric materials that can be thermally evaporated, ZnS, Na₃AlF₆, WO₃ and LaF₃ with refractive index close to the predicted value were selected. As a result, the optimal multilayer OCL consisting of ZnS ($n_1 = 2.4, d_1 = 130 \text{ nm}$)/Na₃AlF₆ ($n_2 = 1.3, d_2 = 60 \text{ nm}$)/WO₃ ($n_3 = 2.0, d_3 = 100 \text{ nm}$)/LaF₃ ($n_4 = 1.6, d_4 = 50 \text{ nm}$) was identified, labeled OCL2 (i.e., star symbol; green color), leading to the maximum achievable improvement in both J_{sc} and AVT as compared to that of the ST-OPVs with a bilayer

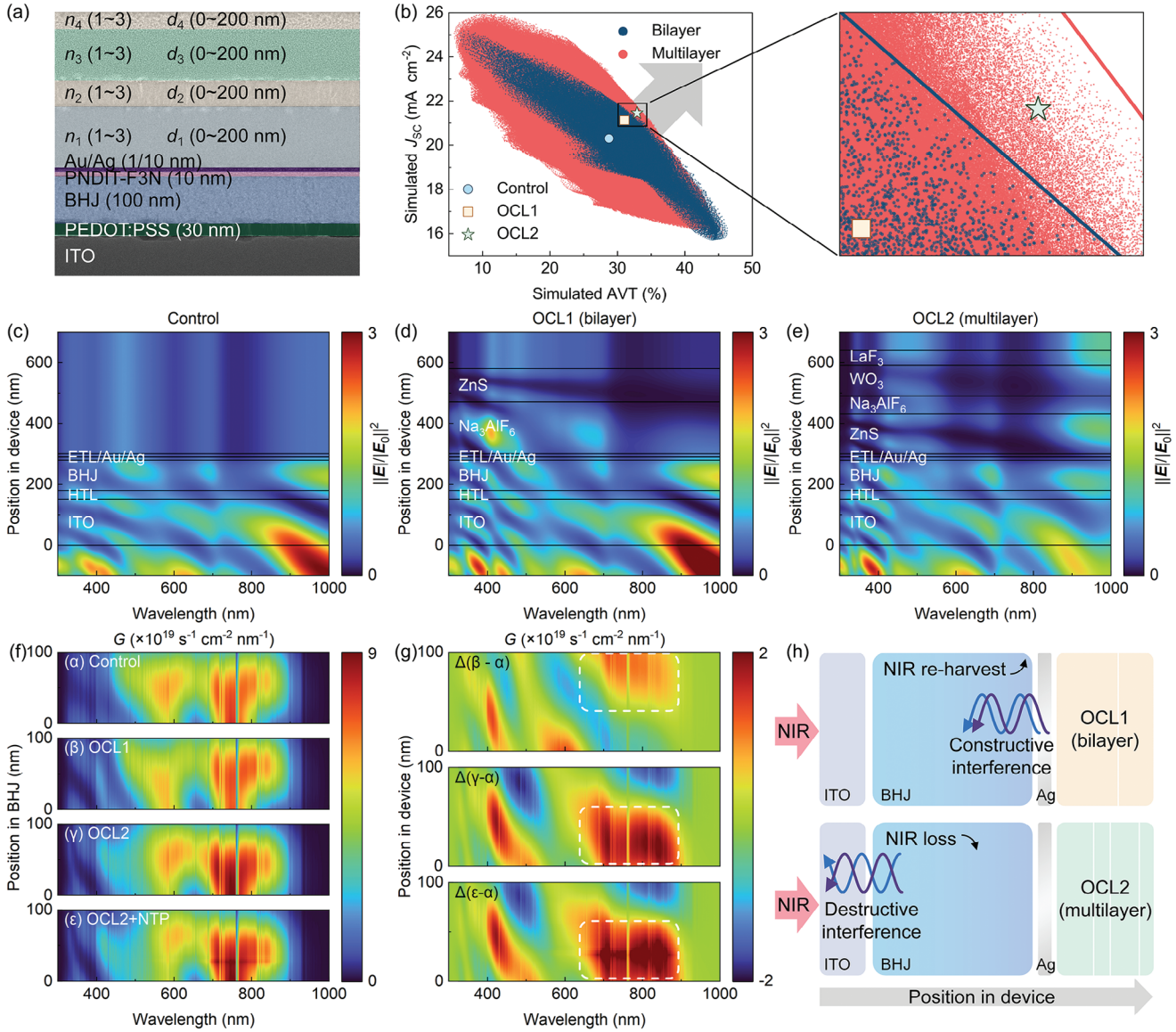


Figure 4. a) Cross-section TEM image of an ST-OPV with a multilayer OCL. b) Left: Contour map of simulated J_{sc} -AVT as a function of the refractive index and layer thickness of the multilayer OCL. The data points in blue represent the simulated results for the ST-OPVs with bilayer OCL and those in red represent the simulated results for the ST-OPVs with multilayer OCL. The circle, square and star symbols in the contour map are the J_{sc} and AVT values calculated for the control device without OCL, the ST-OPV with a bilayer OCL of Na_3AlF_6 (170 nm)/ZnS (110 nm) (OCL1) and that with a multilayer OCL of ZnS (130 nm)/ Na_3AlF_6 (60 nm)/ WO_3 (100 nm)/ LaF_3 50 nm) (OCL2). Right: Magnification of the part from OCL1 to the theoretical maximum. c) Profiles of the electrical field distribution calculated for c) the control ST-OPV without OCL, d) the ST-OPV with OCL1, and e) the ST-OPV with OCL2. f) Exciton generation rate in the BHJ active layer for the control device (labeled α), the ST-OPV with OCL1 (labeled β) and that with OCL2 (labeled γ), and the ST-OPV with both OCL2 and NTP (labeled ϵ). g) The difference in exciton generation rate in the BHJ active layer between the control device and the ST-OPV with OCL1 (labeled $\beta-\alpha$), between the control device and the ST-OPV with OCL2 (labeled $\gamma-\alpha$), and between the control device and the ST-OPV with both OCL2 and NTP (labeled $\epsilon-\alpha$). h) Schematic diagram of the optical coupling mechanisms of bilayer OCL1 and multilayer OCL2.

OCL comprising Na_3AlF_6 ($n_1 = 1.3$, $d_1 = 170$ nm)/ZnS ($n_2 = 2.4$, $d_2 = 110$ nm), labeled OCL1 (i.e., square symbol; yellow color). On the basis of the simulation results, ST-OPVs with bilayer OCL1 and multilayer OCL2 were then fabricated and their structure was examined with cross-sectional TEM and EDS mapping (Figure S24, Supporting Information). Based on the characterization of ST-OPVs with OCL1 or OCL2 and without OCL (Figure S25, Table S6, Supporting Information), the multilayer OCL2 enables

a significantly improved LUE of 4.46% with a PCE of 14.48% and an AVT of 31.1%, simultaneously higher than those of the OCL1-based device and the control device, which is consistent with the theoretical prediction.

Furthermore, the mechanism of optical coupling on the light utilization in ST-OPVs was thoroughly studied by simulating the optical field $|\frac{|E|}{|E_0|}|^2$ distribution and the exciton generation rate

in the devices. The optical field distributions calculated for the control device, the ST-OPV with bilayer OCL1 and that with multilayer OCL2 are shown in Figure 4c–e, respectively. This reveals that both bilayer OCL1 and multilayer OCL2 help enhance light transmission in the visible wavelength range, which is further confirmed by the experimental transmission spectra of the metallic electrodes with OCL1 and OCL2 (Figure S26, Supporting Information). In contrast, different behaviors are observed for NIR light management. The NIR light transmission outside the device scope is suppressed in the OCL1-based device, indicating an enhanced reflection of the NIR photons back to the BHJ active layer for re-harvesting. For the OCL2-based device, a weaker NIR light intensity is found in the ITO section, suggesting a reduced loss of the incident NIR photons. Experimental reflection spectra of the ST-OPVs with OCL2 show weak reflection in the NIR wavelength range comparing with that of the control device, which further confirms the above-simulated results (Figure S27, Supporting Information). To obtain deep insight, the exciton generation rate (G) of the BHJ active layer was subsequently calculated for the control device (labeled α), the ST-OPV with OCL1 (labeled β) and that with OCL2 (labeled γ), as it is shown in Figure 4f. By subtracting G values between the ST-OPV with OCL1 or OCL2 and the control device (Figure 4g), we find that the OCL1-assisted BHJ shows an enhanced exciton generation rate in the NIR wavelength range at the upper area of the BHJ, whereas evident enhancement of the exciton generation rate in the NIR region occurs at the lower area close to the HTL/ITO section for the OCL2-assisted BHJ. Therefore, two different enhancing mechanisms of NIR light utilization are proposed in Figure 4h: 1) enhancement of NIR re-harvesting in the BHJ via enhanced NIR reflection at the BHJ/OCL interface for the bilayer OCL1-based ST-OPV and 2) enhancement of NIR absorption in the BHJ via reduced NIR loss at the ITO/BHJ interface for the multilayer OCL2-based ST-OPV. These results reveal the essence of the optical coupling effect to manipulate the light distribution within the entire device via regulation of the light phase difference at the interface.

2.3. ST-OPVs with the Synergetic NIR Light Management

Taking advantage of the synergetic optical engineering that combines NIR-customized LSPR with the high-throughput computing guided optical coupling effect, PM6:BTP-eC9:L8-BO-based ST-OPVs with a PdCu@Au@SiO₂ NTP-integrated BHJ active layer and a rear multilayer OCL of ZnS(130 nm)/Na₃AlF₆(60 nm)/WO₃(100 nm)/LaF₃(50 nm) were finally fabricated. In addition, a nanostructured AR coating, fabricated as described in Figure S28 (Supporting Information) and optimized as reported in our previous work,^[30] was added to the front glass side of the ST-OPVs to reduce the ambient reflection at the air/glass surface. It should be highlighted that the use of AR coating can enhance the total transmittance of the glass/ITO substrates. The AVT value of glass/ITO substrates was increased from 87.26% to 92.71% after adding the AR coating, as shown in Figure S29 (Supporting Information). Table S7 (Supporting Information) lists the photovoltaic performance of the ST-OPVs with and without nanostructured AR, indicating that the addition of AR can help improve the PCE and AVT.

The J - V characteristics, EQE, and transmission spectra measured for the control device and the optimal ST-OPV with a combination of NTPs, multilayer OCL, and AR are shown in Figure 5a,b, respectively. The corresponding photovoltaic parameters are listed in Table 1. The synergetic strategy of light manipulation results in a breakthrough PCE of 16.14%, an excellent AVT of 33.02%, and an outstanding LUE of 5.33% for the optimal ST-OPVs, significantly outperforming the control device with a PCE of 13.33%, an AVT of 27.40% and a LUE of 3.65%. Such an improvement is explained by the enhancement of the NIR light utilization as demonstrated by a higher EQE over the long wavelength from 700 to 900 nm and the simultaneous enhancement of the optical transmission in the visible wavelength range. The experimental results agree with the simulations shown in Figure 4f,g, in which the exciton generation rate of the BHJ active layer is further enhanced in the NIR wavelength range through the synergetic effect of the NTPs and the multilayer OCL. In addition, the optimal device was encapsulated and sent to the ISO/IEC 17 025:2017 accredited China Photovoltaic Testing Center for certification, which exhibited a PCE of 15.90%, as shown in Figure S30 (Supporting Information). To evaluate the light utilization in ST-OPVs, another figure of merit, the quantum utilization efficiency defined as $QUE(\lambda) = EQE(\lambda) + T(\lambda)$, was calculated.^[64–66] A maximum QUE of 92.1% is observed, higher than that of the control device (87.6%), while the values of QUE are all below the transmittance of ITO/glass (Figure S31, Supporting Information), confirming the reliability of our results. The Commission Internationale de l'Éclairage (CIE) coordinates were then observed to analyze the color neutrality for the control device and the optimal ST-OPV, as shown in Figure 5c, giving comparable positions in the color space. The color rendering index of the optimal ST-OPV is calculated to be 80.2, which is similar to that of the control device (80.6), revealing that the color neutrality is well maintained. Therefore, good visible light transparency and color neutrality can be seen based on the photographs taken for the control device and the optimal ST-OPV (Figure 5d).

Figure 5e shows a comparison of our results with those reported recently by different groups. It is worth noting that the PCE of 16.14% (15.90% certified) represents the best value in ST-OPVs. The LUE of 5.33% is also among the highest values in the literature, demonstrating that the two competing indexes of PCE and AVT have been simultaneously improved to the greatest extent by incorporating synergetic NIR light management. The advantage of such comprehensive optical engineering for high-performance ST-OPVs is equally shown in the spider diagram of Figure 5f, revealing the superior performance of the optimal ST-OPV in PCE, AVT, and LUE to that of the control device. In addition to improving the device performance, the use of an OCL consisting of multilayer dielectric materials has the effect of preventing the permeation of moisture and oxygen into the BHJ active layer, which is beneficial for the long-term stability of ST-OPVs. An aging test was carried out by monitoring the performance of different ST-OPVs that were unencapsulated and stored in an N₂-purged glove box at room temperature. The normalized PCE of the control device and the optimal ST-OPV as a function of the aging time are shown in Figure 5g. After 1000 h, the optimal ST-OPV remains 96% of its initial PCE, higher than that of the control device (86.2%), indicating a $T_{90} > 1000$ h (4500 h fitted by

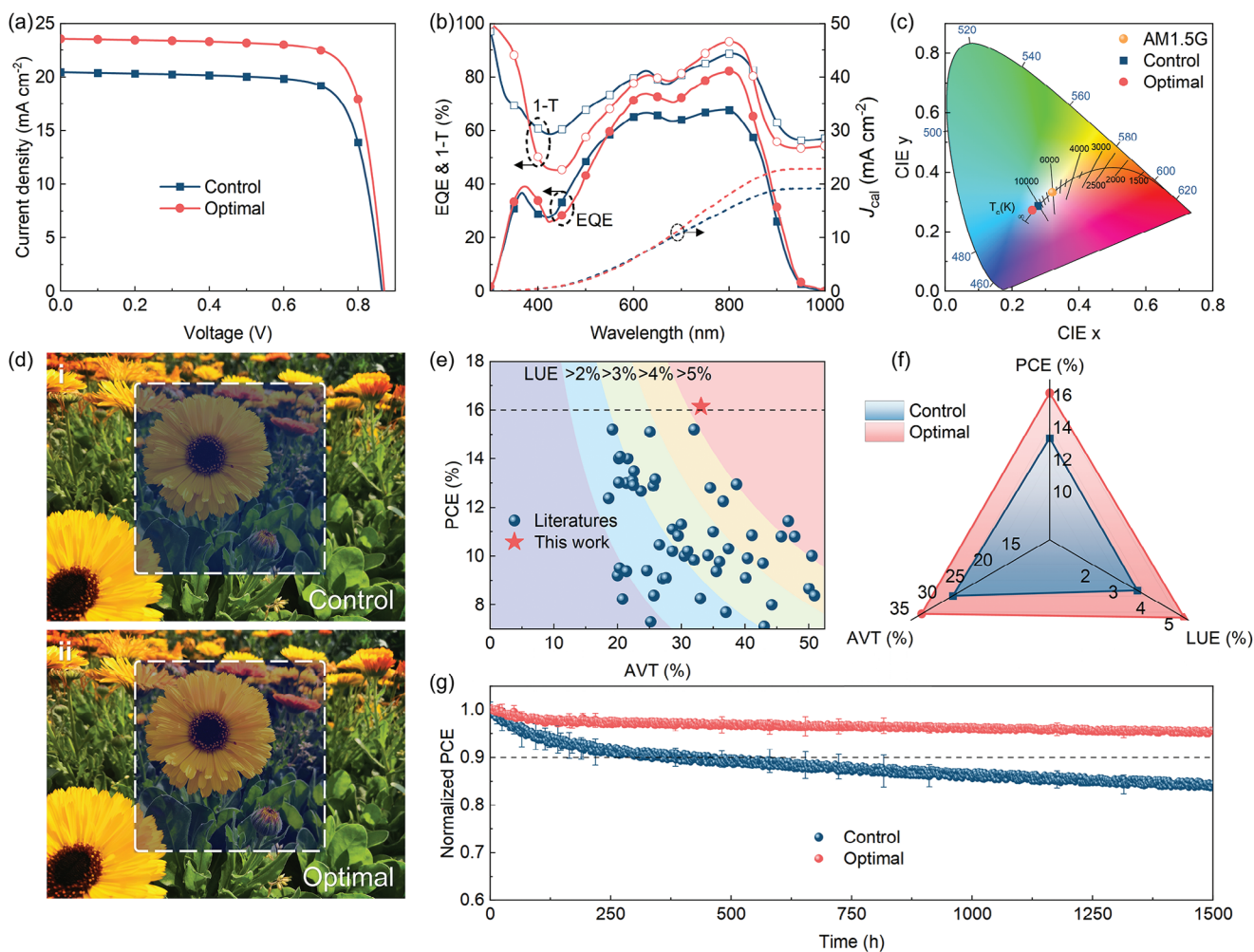


Figure 5. a) J - V characteristics, b) EQE, 1-T and integral short-circuit current spectra, c) chromaticity coordinates measured for the control device and the optimal ST-OPVs with a PdCu@Au@SiO₂ NTP-integrated BHJ active layer, a rear multilayer OCL of ZnS(130 nm)/Na₃AlF₆(60 nm)/WO₃(100 nm)/LaF₃(50 nm) and a front AR coating. d) Photographs of the control device (panel i) and the optimal ST-OPV (panel ii). e) Comparison of the PCE, AVT, and LUE values between the optimal ST-OPVs demonstrated in this work and those reported in the literature listed in Table S8 (Supporting Information). f) Comparison of device performance, including PCE, AVT, and LUE, for the control device and the optimal ST-OPV. g) Long-term stability of the unencapsulated control device and the optimal ST-OPV stored in an N₂-filled glove box.

Table 1. Photovoltaic parameters and semitransparent performance measured for the 100 nm-thick PM6:BTP-eC9:L8-BO (0.6:0.4:0.8)-based control device, the ST-OPVs with a PdCu@Au@SiO₂ NTP-integrated BHJ active layer, the ST-OPVs with a multilayer OCL of ZnS(130 nm)/Na₃AlF₆(60 nm)/WO₃(100 nm)/LaF₃(50 nm) and the optimal ST-OPVs with a combination of a PdCu@Au@SiO₂ NTP-integrated BHJ active layer, a rear multilayer OCL of ZnS(130 nm)/Na₃AlF₆(60 nm)/WO₃(100 nm)/LaF₃(50 nm) and a front AR coating. The photovoltaic results were averaged from the measurements of 10 devices.

Device	J_{sc} [mA cm ⁻²]	J_{cal} [mA cm ⁻²] ^{a)}	V_{oc} [V]	FF [%]	PCE [%]	AVT [%]	LUE [%]	CRI
Control	20.0 ± 0.2	19.2	0.87 ± 0.01	77.1 ± 0.5	13.33 ± 0.11	27.45	3.65	80.62
NTP ^{b)}	21.9 ± 0.2	21.2	0.87 ± 0.01	77.5 ± 0.2	14.66 ± 0.12	27.40	4.02	80.61
OCL ^{c)}	21.1 ± 0.5	20.6	0.87 ± 0.01	78.8 ± 0.2	14.48 ± 0.32	31.12	4.46	80.05
Optimal ^{d)}	23.6 ± 0.4	22.9	0.87 ± 0.01	78.7 ± 0.5	16.14 ± 0.17	33.02	5.33	80.21

^{a)} J_{cal} is the calculated short circuit current density from EQE spectra using the following equation: $J_{cal} = \int \frac{EQE(\lambda)F(\lambda)\lambda e}{hc} d\lambda$, where e is the elementary charge, h is the Planck constant, c is the speed of light; ^{b)} ST-OPVs with a PdCu@Au@SiO₂ NTP-integrated BHJ active layer (0.1 wt.%); ^{c)} ST-OPVs with a rear multilayer OCL of ZnS (130 nm)/Na₃AlF₆ (60 nm)/WO₃ (100 nm)/LaF₃ (50 nm); ^{d)} Optimal ST-OPVs with a combination of a PdCu@Au@SiO₂ NTP-integrated BHJ active layer (0.1 wt.%), a rear multilayer OCL of ZnS (130 nm)/Na₃AlF₆ (60 nm)/WO₃ (100 nm)/LaF₃ (50 nm) and a front AR coating.

linear extrapolation), which is significantly improved compared with that of the control device (400 h).

3. Conclusion

To summarize, a combination of NIR-customized LSPR via deliberately synthesized core–birefractive shell NTPs and a multilayer OCL designed by high-throughput optical screening was developed to optimize the performance of the ST-OPVs over the two competing indexes of PCE and AVT to the maximum extent. PM6:BTP-eC9:L8-BO-based ST-OPVs with a PdCu@Au@SiO₂ NTP-integrated BHJ active layer and a multilayer OCL of ZnS(130 nm)/Na₃AlF₆(60 nm)/WO₃(100 nm)/LaF₃(50 nm) show a record-PCE of 16.14% (certified as 15.90%) along with an excellent AVT of 33.02%, leading to a remarkable LUE of 5.33% with an ≈50% enhancement compared to the counterpart device without synergetic optical engineering. The optical design presented in this work provides an encouraging and universal approach for promoting breakthroughs in ST-OPVs toward the practical applications of building-integrated photovoltaics and self-powered greenhouses.

4. Experimental Section

Materials: PM6, BTP-eC9, L8-BO, and PNDIT-F3N were purchased from Organtec Ltd. PEDOT: PSS solution (Clevios PVP 4083) was purchased from Heraeus. Na₃AlF₆ was purchased from Macklin. ZnS, WO₃, and LaF₃ were purchased from Adamas. The following reagents were purchased from Sigma-Aldrich, including sodium tetrachloropalladate(II) (Na₂PdCl₄, 99%), copper(II) chloride dihydrate (CuCl₂·2H₂O, 99%), tetraethoxysilane (TEOS, 99%), ammonium hydroxide (NH₄OH, 25% in water), ascorbic acid (AA, 99%), potassium bromide (KBr, 99%), octadecyltrimethoxysilane (OTMS, 90%), gold(III) chloride trihydrate (HAuCl₄·3H₂O, 99.9%), polyvinylpyrrolidone (PVP, MW 55 000, 99%), absolute ethanol (99%), chloroform (CHCl₃, 99%) and 1,8-diiodooctane (DIO, 99%). All chemicals and reagents were used as received.

Synthesis of the PdCu@Au@SiO₂ NTPs: 1) Synthesis of the PdCu seeds: In a typical process, 3 mg of CuCl₂·2H₂O, 20 mg of ascorbic acid, 35 mg of PVP_{55k}, and 300 mg of KBr were dissolved in 3 mL of ultrapure water. The solution was heated in an oil bath set to 80 °C under magnetic stirring. After 10 min, 1 mL of an aqueous Na₂PdCl₄ solution (19 mg mL⁻¹) was quickly injected in the reaction medium. The solution was prepared at least 1 h before use. After 2 h of reaction at 80 °C, the obtained PdCu seeds were collected via centrifugation (12 000 g, 30 min) and washed three times with a solution of PVP (2 g L⁻¹) to remove precursors in excess. Finally, the PdCu seeds were re-dispersed in an aqueous solution of PVP (5 mL). 2) Synthesis of the PdCu@Au NTPs: First, 140 mg of ascorbic acid, 24 mg of PVP_{55k}, and 100 μL of the stock solution of PdCu seeds were added successively to 5 mL of water in a 50 mL flask under vigorous stirring. After 10 min, HAuCl₄ (20 mL, 0.5 mM) was added to the dispersion with a syringe pump at a rate of 5 mL h⁻¹ at room temperature. Once finished, the dispersion was centrifuged and re-dispersed in deionized water once and twice with ethanol (10 min at 9000 g). Finally, the particles were re-dispersed in 2 mL of ethanol, forming the PdCu@Au NTPs. 3) Synthesis of the PdCu@Au@SiO₂ NTPs: PdCu@Au NTPs were centrifuged at 9000 g for 10 min and washed three times with a solution of PVP (2 g L⁻¹) in ethanol. Then, they were transferred to chloroform by centrifugation at 9000 g (10 min). 28.3 μL of ammonia solution (25%) and a given volume μL of TEOS solution (10%, v/v in ethanol) were added to 500 μL of the gold tripods ([Au⁰] = 3.1 mM) dispersed in absolute ethanol, under vigorous stirring. Stirring was maintained for 1 h in an ultra-sound bath (25 °C) and then overnight under a conventional magnetic plate. The dispersion of silica-coated tripods was washed once with DI water and

twice with ethanol (9000 g, 10 min). A fully and thin continuous silica shell was achieved with a volume of 5 μL TEOS. Then, 30 μL of NH₄OH (25%, v/v) and 150 μL of OTMS solution (10%, v/v in chloroform) were sequentially added to 1 mL of PdCu@Au@SiO₂ dispersion (3.1 mM in Au) for post-functionalization, to ensure good dispersion and colloidal stability in chloroform. After stirring for 24 h, the resulting PdCu@Au@SiO₂ NTPs were washed twice with a solution of chloroform/ethanol (1/1, v/v) and twice with chloroform. The tripods were finally dispersed in chloroform.

Device Fabrication: The ITO/glass substrates (15 Ω sq⁻¹) were cleaned using ultrasonication sequentially with detergent, deionized water, acetone, and isopropyl alcohol, each for 30 min. After wet cleaning, the ITO/glass substrates were exposed to plasma treatment for 5 min prior to device fabrication. A 30 nm-thick PEDOT: PSS HTL was deposited on the ITO/glass substrates using spin-coating at a rotation speed of 3000 rpm for 60 s, followed by annealing at 130 °C for 20 min in air. The PEDOT: PSS solution was modified in advance by an Nb₂C MXene (1.0 wt.%) aqueous solution. The PM6:BTP-eC9:L8-BO mixture solutions (16 mg mL⁻¹) with different weight ratios of PM6 to BTP-eC9 to L8-BO, dissolved in chloroform and with a 0.5 v% of DIO additive, were stirred for 24 h to prepare the ternary BHJ active layer. PM6:BTP-eC9:L8-BO BHJ active layers were then deposited on the PEDOT: PSS HTL by using spin-coating at a rotation speed of 6000 rpm for 30 s, followed by annealing at 100 °C for 10 min in a glove box with O₂ and H₂O levels < 0.1 ppm. Subsequently, a 10 nm-thick PNDIT-F3N ETL (0.95 mg mL⁻¹ in methanol with 5 v% acetic acid cosolvent) was deposited on the BHJ active layer by spin-coating at a rotation speed of 3000 rpm for 30 s. A bilayer Au (1.0 nm)/Ag (10 nm) upper electrode was deposited by thermal evaporation in a vacuum system (<5 × 10⁻⁴ Pa). The evaporation rate for Au was 0.1 Å s⁻¹ and that for Ag was 1.0 Å s⁻¹. The multilayered OCL of ZnS(130 nm)/ Na₃AlF₆ (60 nm)/WO₃ (100 nm)/LaF₃ (50 nm) was then deposited on the upper electrode using thermal evaporation, at an evaporation rate of 2.0 Å s⁻¹ for each layer. The nanostructured AR coating was finally stuck upon the front side of the glass substrates. The active area of the ST-OPVs was 4.14 mm², defined by an aperture mask. The devices were finally encapsulated within glass casings using a layer of UV glue that effectively sealed any gaps present.

Characterizations: All transmission, absorption, and reflection spectra were measured using a UV-vis spectrophotometer (MAPADA UV-1800 PC). The CIE 1931 color coordinates of the ST-OPVs were obtained using a PR-655 spectroradiometer (Photo Research). The surface morphologies of the BHJ films with and without NTPs were analyzed using AFM (Bruker Dimension Icon). The SEM images were obtained using a ZEISS Sigma 500 microscope. The TEM and EDS images were obtained by using a Themis ETEM G3 microscope. The Raman spectra were measured by a 3D confocal Raman microscope (Nano Finder 30A), excited by a 532 nm laser. The Raman mappings were measured with an area of 2 μm × 2 μm and a step size of 0.4 μm, probed at 1425 cm⁻¹. Electrochemical impedance spectroscopy was measured using a bipotentiostat (Corrtest CS2350H) with a bias of 0.8 V over the frequency range from 0.1 Hz to 1 MHz in the dark state. The GIWAXS measurements were performed using an incident angle of 0.15° at the BL14B station of the Shanghai Synchrotron Radiation Facility. TA spectroscopy was performed using a pump-probe system. The amplifier generated a 1030 nm pulse with a repetition rate of 100 kHz, a duration of 300 fs, and an energy of 50 mJ per pulse. The pulse was then divided into two parts using a beam splitter. One was introduced to an optical parametric amplifier to produce a certain wavelength for the pump beam (675 nm, 10 μJ cm⁻²), and the other was focused onto a YAG plate to generate a white light continuum as the probe beam. The transmitted probe light from the sample was collected by a CCD sensor.

The J–V characteristics of the ST-OPVs were measured using an AM1.5G solar simulator (Newport Oriel Sol3A) (100 mW cm⁻²) and a source meter (Keithley 2420). The solar simulator was calibrated using a standard monocrystalline silicon reference cell (Oriel model 91 150 V). The EQE spectra were measured using a 7-SCSpec solar cell measurement system (7-STAR Co.). The stability of the as-prepared ST-OPVs was monitored in an N₂-purged glove box with moisture and oxygen levels below 0.1 ppm at 25 °C.

Theoretical Simulation: The optical profiles in different ST-OPVs were calculated using COMSOL Multiphysics. The device configuration was ITO(150 nm)/PEDOT:PSS(30 nm)/BHJ(100 nm)/PNDIT-F3N(10 nm)/Au(1 nm)/Ag(10 nm). The simulation was operated on the Kunwu intelligent computational materials platform of Zhijiang Lab. Optical constants for functional layers were measured using a spectroscopic ellipsometer (J.A. Woollam RC2-XI).

The wavelength-dependent transmission, $T(\lambda)$, absorption, $A(\lambda)$, and profile of the electric field, $E(x, \lambda)$, in the ST-OPVs with different OCLs were simulated using the TMM method over the wavelength range from 300 to 1000 nm. The exciton generation rate (G) was calculated using the following equation:

$$G = \frac{2\pi\epsilon_0nkF(\lambda)}{h} \left| \frac{|E(x, \lambda)|}{|E_0(x, \lambda)|} \right|^2 \quad (3)$$

where ϵ_0 is the vacuum permittivity, n , and k are the wavelength dependent refractive index and extinction coefficient of the active layer, $F(\lambda)$ is the AM1.5G irradiation, x is the position along the electric field in the active layer and h is the Planck constant. The exciton generation rate of the BHJ active layer integrated with NTPs in the ST-OPVs with a multilayer OCL was calculated using COMSOL multiphysics. The 3D optical field intensity was reduced to a 1D profile along the Z direction using the averaging method along the other axis, as shown in Figure S32 (Supporting Information).

In high-throughput computing, refractive indexes for OCL materials were regarded as constants and ranged from 1.0 to 3.0, with an interval of 0.2. The thickness of the OCL ranged from 0 to 200 nm, with an interval of 10 nm. In total, the performance of 47 064 402 ST-OPVs with different OCL combinations of $n_1, n_2, n_3, n_4, d_1, d_2, d_3$ and d_4 was analyzed for J_{SC} and AVT. The simulation was operated using python language on a server (Intel(R) Xeon(R) Silver 4216 CPU @ 2.10 GHz, 256 GB).

Supporting Information

Supporting Information is available from the Wiley Online Library or from the author.

Acknowledgements

This work was financially supported by the open research fund of Songshan Lake Materials Laboratory (No. 2021SLABFK09) and the National Natural Science Foundation of China (12174244). S.W. acknowledges funding support from the Program for Professor of Special Appointment (Eastern Scholar) at the Shanghai Institutions of Higher Learning and the Shanghai Rising-Star Program (19QA1403800). R.B. thanks the NANO-PHOT Graduate School for support (ANR-18-EURE-0013). Y.B.Q. acknowledges the support from the Energy Materials and Surface Sciences Unit of the Okinawa Institute of Science and Technology Graduate University. The authors gratefully acknowledge Teresa Hungria for assistance in TEM characterization, Clément Vecco-Garda for assistance in the synthesis of NTPs, and Minyu Chen for assistance in the scattering measurement.

Conflict of Interest

There are no conflicts to declare.

Data Availability Statement

The data that support the findings of this study are available from the corresponding author upon reasonable request.

Keywords

high-throughput optical screening, near-infrared absorption enhancement, optical engineering, plasmonics, semitransparent organic photovoltaics

- [1] C. Ballif, L.-E. Perret-Aebi, S. Lufkin, E. Rey, *Nat. Energy* **2018**, *3*, 438.
- [2] Y. Li, X. Guo, Z. Peng, B. Qu, H. Yan, H. Ade, M. Zhang, S. R. Forrest, *Proc. Natl. Acad. Sci. U. S. A.* **2020**, *117*, 21147.
- [3] I. Burgués-Ceballos, L. Lucera, P. Tiwana, K. Ocytko, L. W. Tan, S. Kowalski, J. Snow, A. Pron, H. Bürckstümmer, N. Blouin, G. Morse, *Joule* **2021**, *5*, 2261.
- [4] N. Liang, R. Tian, Y. Xu, H. Yao, H. Yang, Y. Wei, X. Xin, R. Chen, T. Zhai, Z. Wang, J. Hou, *Adv. Mater.* **2023**, *35*, 2300360.
- [5] X. Wu, S. Liu, H. Li, X. Meng, X. Hu, R. Guo, Y. Chen, *Adv. Opt. Mater.* **2022**, *10*, 2201803.
- [6] Y. Li, X. Huang, H. K. M. Sheriff, S. R. Forrest, *Nat. Rev. Mater.* **2022**, *8*, 186.
- [7] H. Cheng, Y. Zhao, Y. Yang, *Adv. Energy Mater.* **2022**, *12*, 2102908.
- [8] C. J. Traverse, R. Pandey, M. C. Barr, R. R. Lunt, *Nat. Energy* **2017**, *2*, 849.
- [9] O. Almora, D. Baran, G. C. Bazan, C. I. Cabrera, S. Erten-Ela, K. Forberich, F. Guo, J. Hauch, A. W. Y. Ho-Baillie, T. J. Jacobsson, R. A. J. Janssen, T. Kirchartz, N. Kopidakis, M. A. Loi, R. R. Lunt, X. Mathew, M. D. McGehee, J. Min, D. B. Mitzi, M. K. Nazeeruddin, J. Nelson, A. F. Nogueira, U. W. Paetzold, B. P. Rand, U. Rau, H. J. Snaith, E. Unger, L. Vaillant-Roca, C. Yang, H. Yip, et al., *Adv. Energy Mater.* **2023**, *13*, 2203313.
- [10] Y. Zhang, J. Zheng, Z. Jiang, X. He, J. Kim, L. Xu, M. Qin, X. Lu, A. K. K. Kyaw, W. C. H. Choy, *Adv. Energy Mater.* **2023**, *13*, 2203266.
- [11] B. Deng, Y. Shen, K. Zheng, C. Wang, G. Lévêque, T. Xu, *Sol. RRL* **2023**, *7*, 2300211.
- [12] S. Guan, Y. Li, K. Yan, W. Fu, L. Zuo, H. Chen, *Adv. Mater.* **2022**, *34*, 2205844.
- [13] J. Jing, S. Dong, K. Zhang, Z. Zhou, Q. Xue, Y. Song, Z. Du, M. Ren, F. Huang, *Adv. Energy Mater.* **2022**, *12*, 2200453.
- [14] W. Liu, S. Sun, S. Xu, H. Zhang, Y. Zheng, Z. Wei, X. Zhu, *Adv. Mater.* **2022**, *34*, 2200337.
- [15] W. Liu, S. Sun, L. Zhou, Y. Cui, W. Zhang, J. Hou, F. Liu, S. Xu, X. Zhu, *Angew. Chem., Int. Ed.* **2022**, *61*, e202116111.
- [16] D. Wang, H. Liu, Y. Li, G. Zhou, L. Zhan, H. Zhu, X. Lu, H. Chen, C.-Z. Li, *Joule* **2021**, *5*, 945.
- [17] T. Chen, S. Li, Y. Li, Z. Chen, H. Wu, Y. Lin, Y. Gao, M. Wang, G. Ding, J. Min, Z. Ma, H. Zhu, L. Zuo, H. Chen, *Adv. Mater.* **2023**, *35*, 2300400.
- [18] S. Yoon, S. Park, S. H. Park, S. Nah, S. Lee, J.-W. Lee, H. Ahn, H. Yu, E.-Y. Shin, B. J. Kim, B. K. Min, J. H. Noh, H. J. Son, *Joule* **2022**, *6*, 2406.
- [19] J. Wang, M. Zhang, J. Lin, Z. Zheng, L. Zhu, P. Bi, H. Liang, X. Guo, J. Wu, Y. Wang, L. Yu, J. Li, J. Lv, X. Liu, F. Liu, J. Hou, Y. Li, *Energy Environ. Sci.* **2022**, *15*, 1585.
- [20] W. Lan, J. Gu, S. Wu, Y. Peng, M. Zhao, Y. Liao, T. Xu, B. Wei, L. Ding, F. Zhu, *EcoMat* **2021**, *3*, e12134.
- [21] Y. Cui, Y. Xu, H. Yao, P. Bi, L. Hong, J. Zhang, Y. Zu, T. Zhang, J. Qin, J. Ren, Z. Chen, C. He, X. Hao, Z. Wei, J. Hou, *Adv. Mater.* **2021**, *33*, 2102420.
- [22] D.-D. Zhang, X.-C. Jiang, R. Wang, H.-J. Xie, G.-F. Ma, Q.-D. Ou, Y.-L. Chen, Y.-Q. Li, J.-X. Tang, *ACS Appl. Mater. Interfaces* **2013**, *5*, 10185.

- [23] R. Betancur, P. Romero-Gomez, A. Martinez-Otero, X. Elias, M. Maymó, J. Martorell, *Nat. Photonics* **2013**, *7*, 995.
- [24] X. Liu, Z. Zhong, R. Zhu, J. Yu, G. Li, *Joule* **2022**, *6*, 1918.
- [25] L. Xiao, G. Huang, H. Zhang, X. Zhang, Y. Li, S. Li, T. Jiang, B. Han, Y. Zhang, H. Zhou, *Sol. RRL* **2022**, *6*, 2100818.
- [26] Y. Li, C. Ji, Y. Qu, X. Huang, S. Hou, C. Li, L. Liao, L. J. Guo, S. R. Forrest, *Adv. Mater.* **2019**, *31*, 1903173.
- [27] Y. Bai, C. Zhao, X. Chen, S. Zhang, S. Zhang, T. Hayat, A. Alsaedi, Z. Tan, J. Hou, Y. Li, *J. Mater. Chem. A* **2019**, *7*, 15887.
- [28] T. Xu, Y. Luo, S. Wu, B. Deng, S. Chen, Y. Zhong, S. Wang, G. Lévêque, R. Bachelot, F. Zhu, *Adv. Sci.* **2022**, *9*, 2202150.
- [29] R. Xia, C. J. Brabec, H.-L. Yip, Y. Cao, *Joule* **2019**, *3*, 2241.
- [30] X. Rodríguez-Martínez, E. Pascual-San-José, M. Campoy-Quiles, *Energy Environ. Sci.* **2021**, *14*, 3301.
- [31] T. Xu, B. Deng, Y. Zhao, Z. Wang, G. Lévêque, Y. Lambert, B. Grandidier, S. Wang, F. Zhu, *Adv. Energy Mater.* **2023**, *13*, 2301367.
- [32] S. Lie, A. Bruno, L. H. Wong, L. Etgar, *ACS Appl. Mater. Interfaces* **2022**, *14*, 11339.
- [33] K. Yao, H. Zhong, Z. Liu, M. Xiong, S. Leng, J. Zhang, Y. Xu, W. Wang, L. Zhou, H. Huang, A. K.-Y. Jen, *ACS Nano* **2019**, *13*, 5397.
- [34] T. Kim, H. Kang, S. Jeong, D. J. Kang, C. Lee, C.-H. Lee, M.-K. Seo, J.-Y. Lee, B. J. Kim, *ACS Appl. Mater. Interfaces* **2014**, *6*, 16956.
- [35] H. A. Atwater, A. Polman, *Nat. Mater.* **2010**, *9*, 205.
- [36] V. Janković, Y. M. Yang, J. You, L. Dou, Y. Liu, P. Cheung, J. P. Chang, Y. Yang, *ACS Nano* **2013**, *7*, 3815.
- [37] S.-W. Baek, G. Park, J. Noh, C. Cho, C.-H. Lee, M.-K. Seo, H. Song, J.-Y. Lee, *ACS Nano* **2014**, *8*, 3302.
- [38] S. Liu, R. Jiang, P. You, X. Zhu, J. Wang, F. Yan, *Energy Environ. Sci.* **2016**, *9*, 898.
- [39] Y. Zhao, K. Zheng, J. Ning, T. Xu, S. Wang, *ACS Appl. Electron. Mater.* **2023**, *5*, 632.
- [40] B. Wu, X. Wu, C. Guan, K. Fai Tai, E. K. L. Yeow, H. Jin Fan, N. Mathews, T. C. Sum, *Nat. Commun.* **2013**, *4*, 2004.
- [41] C. Hanske, M. N. Sanz-Ortiz, L. M. Liz-Marzán, *Adv. Mater.* **2018**, *30*, 1707003.
- [42] T. Ye, S. Ma, X. Jiang, L. Wei, C. Vijila, S. Ramakrishna, *Adv. Funct. Mater.* **2017**, *27*, 1606545.
- [43] H. Choi, J.-P. Lee, S.-J. Ko, J.-W. Jung, H. Park, S. Yoo, O. Park, J.-R. Jeong, S. Park, J. Y. Kim, *Nano Lett.* **2013**, *13*, 2204.
- [44] Z. Hu, J. Wang, Z. Wang, W. Gao, Q. An, M. Zhang, X. Ma, J. Wang, J. Miao, C. Yang, F. Zhang, *Nano Energy* **2019**, *55*, 424.
- [45] X. Zheng, L. Zuo, K. Yan, S. Shan, T. Chen, G. Ding, B. Xu, X. Yang, J. Hou, M. Shi, H. Chen, *Energy Environ. Sci.* **2023**, *16*, 2284.
- [46] B. Deng, H. Lian, B. Xue, R. Song, S. Chen, Z. Wang, T. Xu, H. Dong, S. Wang, *Small* **2023**, *19*, 2207505.
- [47] C. Han, J. Wang, S. Zhang, L. Chen, F. Bi, J. Wang, C. Yang, P. Wang, Y. Li, X. Bao, *Adv. Mater.* **2023**, *35*, 2208986.
- [48] T. Li, S. Dai, Z. Ke, L. Yang, J. Wang, C. Yan, W. Ma, X. Zhan, *Adv. Mater.* **2018**, *30*, 1705969.
- [49] X. Huang, L. Zhang, Y. Cheng, J. Oh, C. Li, B. Huang, L. Zhao, J. Deng, Y. Zhang, Z. Liu, F. Wu, X. Hu, C. Yang, L. Chen, Y. Chen, *Adv. Funct. Mater.* **2022**, *32*, 2108634.
- [50] B. Pang, Y. Zhao, H. Luehmann, X. Yang, L. Detering, M. You, C. Zhang, L. Zhang, Z.-Y. Li, Q. Ren, Y. Liu, Y. Xia, *ACS Nano* **2016**, *10*, 3121.
- [51] C. Xue, X. Chen, S. J. Hurst, C. A. Mirkin, *Adv. Mater.* **2007**, *19*, 4071.
- [52] P. Du, P. Jing, D. Li, Y. Cao, Z. Liu, Z. Sun, *Small* **2015**, *11*, 2454.
- [53] P. Mulvaney, *Langmuir* **1996**, *12*, 788.
- [54] H. Benisty, J.-J. Greffet, P. Lalanne, *Introduction to Nanophotonics*, Oxford University Press, Oxford, England, **2022**.
- [55] V. Juvé, M. F. Cardinal, A. Lombardi, A. Crut, P. Maioli, J. Pérez-Juste, L. M. Liz-Marzán, N. Del Fatti, F. Vallée, *Nano Lett.* **2013**, *13*, 2234.
- [56] H. Moosmüller, W. P. Arnott, *J. Air Waste Manage. Assoc.* **2009**, *59*, 1028.
- [57] T. Xu, C. Gong, S. Wang, H. Lian, W. Lan, G. Lévêque, B. Grandidier, J. Plain, R. Bachelot, B. Wei, F. Zhu, *Sol. RRL* **2020**, *4*, 1900522.
- [58] C. Awada, T. Popescu, L. Douillard, F. Charra, A. Perron, H. Yockell-Lelièvre, A.-L. Baudrion, P.-M. Adam, R. Bachelot, *J. Phys. Chem. C* **2012**, *116*, 14591.
- [59] B. Lindner, F. Foschum, A. Kienle, *Appl. Opt.* **2022**, *61*, 2775.
- [60] G. Lozano, G. Grzela, M. A. Verschuuren, M. Ramezani, J. G. Rivas, *Nanoscale* **2014**, *6*, 9223.
- [61] A. K. K. Kyaw, D. H. Wang, V. Gupta, W. L. Leong, L. Ke, G. C. Bazan, A. J. Heeger, *ACS Nano* **2013**, *7*, 4569.
- [62] H. Lian, M. Pan, J. Han, X. Cheng, J. Liang, W. Hua, Y. Qu, Y. Wu, Q. Dong, B. Wei, H. Yan, W.-Y. Wong, *J. Mater. Chem. A* **2021**, *9*, 16500.
- [63] J. Wang, Y. Wang, P. Bi, Z. Chen, J. Qiao, J. Li, W. Wang, Z. Zheng, S. Zhang, X. Hao, J. Hou, *Adv. Mater.* **2023**, *35*, 2301583.
- [64] R. Xia, H. Gu, S. Liu, K. Zhang, H.-L. Yip, Y. Cao, *Sol. RRL* **2019**, *3*, 1800270.
- [65] X. Huang, Y. Cheng, Y. Fang, L. Zhang, X. Hu, S. Y. Jeong, H. Zhang, H. Y. Woo, F. Wu, L. Chen, *Energy Environ. Sci.* **2022**, *15*, 4776.
- [66] Z. Hu, J. Wang, X. Ma, J. Gao, C. Xu, K. Yang, Z. Wang, J. Zhang, F. Zhang, *Nano Energy* **2020**, *78*, 105376.